ELSEVIER

International Journal of Heat and Fluid Flow 23 (2002) 317–329

International Journal of HEAT AND FLUID FLOW

www.elsevier.com/locate/ijhff

The influence of source terms on a gradient-based curvilinear grid scheme applied to a reacting flow ☆

George M. Lloyd [a,*], A. Razani [b], Kwang J. Kim [c,1]

[a] Department of Civil and Materials Engineering, University of Illinois at Chicago, 842 West Taylor Street, Chicago, IL 60607, USA
[b] University of New Mexico, Department of Mechanical Engineering, Albuquerque, NM 87131, USA
[c] Department of Mechanical Engineering, University of Nevada, Reno, NV 89557, USA

Abstract

One-dimensional simulations provide an appropriate level of detail for studying the reactor dynamics of gas–solid metal hydride absorption heat pumps, which are a class of reacting flows. Because of the high energy densities and consequent difficulty in optimizing the reactors for finite time thermal performance, steep concentration gradients develop near energy transfer boundaries. With a uniform and fixed grid capable of resolving the gradients, the computational cost of a simulation can be considerable. Adaptive grid methods have been shown to reduce the computational cost in several classes of problems by reducing the overall discretization error compared to fixed grids using the same number of nodes through redistribution of node density. However the class of problems including mass and energy source terms, which are a prominent feature in reacting flows, are not well represented in the literature. In this paper an adaptive moving grid formulation is developed for a model of a metal hydride heat pump and the influence of the source terms evaluated. The grid satisfies an elliptic mesh equation to ensure smoothness, and grid motion is determined by a gradient-based logarithmic weight function of the absorbed hydrogen concentration, which avoids grid collapse. The strategy is shown to improve the resolution of monotonic gradients near heat transfer boundaries. The scheme performs less well when features exhibiting curvature appear simultaneously. © 2002 Published by Elsevier Science Inc.

Keywords: Adaptive finite difference method; Metal hydride; Heat pump; Reacting flow

1. Introduction

The heat and mass transfer processes in many energy conversion systems such as absorption heat pumps produce large concentration gradients. These gradients accompany moving reaction fronts during cyclical operation (Frauhammer et al., 1998), and have their origin in the high energy density of the absorbants, and correspondingly high local heat fluxes associated with finite power operation. Resolving the reactor dynamics in the neighborhood of these gradients is important because most absorption and desorption occurs there. Similar phenomenology arises in other fields, such as electrochemistry (Bieniaz, 1993), phase change problems (Mackenzie and Robertson, 2000), and inertial confinement fusion simulations (Yasar and Moses, 1992).

An example of such a system is a two-reactor five-step refrigeration cycle (see Fig. 1a) realized using high energy density metal hydride reactors. The design and characterization of recent reactors is described in Kim et al. (1998). A computational simulation of this system, which formed an integral part of the reactor optimization program, is shown in Fig. 1b, illustrating the concentration gradients which initiate and develop, particularly in the regenerator. Peak gradients in the latter phase exceed 5×10^3 (m^{-1}). This modeling used constant mesh spacing on a fixed grid, as described in (Lloyd et al. 1998,1999; Lloyd, 1998), as has been common in these types of purely Eulerian simulations.

Achieving fidelity in these calculations requires a fine mesh in regions of large gradients and curvature, necessitating a uniformly spaced mesh with many grid points—a computationally expensive approach—or a

☆ This paper is a revised and expanded version of a paper presented at CHT'01, the Second International Symposium on Advances in Computational Heat Transfer (Palm Cove, Qld., Australia, 20–25 May 2001), the proceedings of which were published by Begell House, Inc.

* Corresponding author. Tel.: +1-312-996-3441; fax: +1-312-996-2426.

E-mail addresses: glloyd@uic.edu (G.M. Lloyd), razani@unm.edu (A. Razani), kwangkim@unr.edu (K.J. Kim).

[1] Tel.: 775-784-7522/6931.

0142-727X/02/$ - see front matter © 2002 Published by Elsevier Science Inc.
PII: S0142-727X(02)00179-0

Nomenclature

A	reaction prefactor ($kmol_H/kmol_h$ s)
c	heat capacity (W s/kg K)
E_a	activation energy ($J/kmol_{H_2}$)
g	heat generation term ($J/s\,m^3_{(c)}$)
h_∞	heat transfer coefficient (W/m^2 C)
$h_{c_{sw}}$	solid-phase/wall heat transfer coefficient
$h_{c_{fw}}$	fluid-phase/wall heat transfer coefficient
h_{sf}	interstitial heat transfer coefficient
$\mathscr{J}$	grid jacobian
k_{eff}	effective thermal conductivity (W/m K)
k_f	thermal conductivity H_2 (W/m K)
K	permeability (m^2)
N	number of nodes
Nu_D	interstitial Nusselt number based upon particle diameter, $h_{sf}D/k_f$
$p_{eq\,H_2}$	equilibrium hydride pressure (N/m^2)
$\bar{R}$	perfect gas constant 8314 (J/kmol K)
t_s	time coordinate (s)
T_s	temperature function for solid phase (K)
T	temperature function for fluid phase (K)
$T_w(t)$	average wall temperature (K)
T_{cold}	temperature of cold reservoir (°C)
T_{hot}	temperature of hot reservoir (°C)
v	Darcy filtration velocity (m/s)
x	absorbed hydrogen concentration ($kmol_H/kmol_h$)
$x_{\alpha_{max}}$ to $x_{\beta_{min}}$	plateau region of the metal hydride
δr	energy deposition depth (m)
$dA_{sf}/dV_{(c)}$	specific surface area ($m^2/m^3_{(c)}$)
α_v	volumetric heat transfer coefficient (W/m^3 K)
β	grid constant
μ	viscosity (Pa s)
γ	molecular weight (kg/kmol)
ϕ	porosity ($m^3_{pore}/m^3_{(c)}$)
$\dot{\varphi}$	field source term for hydrogen ($kgH_2/m^3_{(c)}$ s)
$\wp$	hydride density ($particles_h/m^3_{(c)}$)

Superscripts and accents

$'$	refers to regenerator property
i	pertaining to the i-phase
$f^{\llcorner n}$, $f^{\llcorner n}_{\llcorner i}$	discrete value of f at time step n (and node i)

Subscripts

(c)	refers to continuum
H_2	hydrogen
R	reactor
w	reactor wall

Acronyms

LTE	local thermal equilibrium

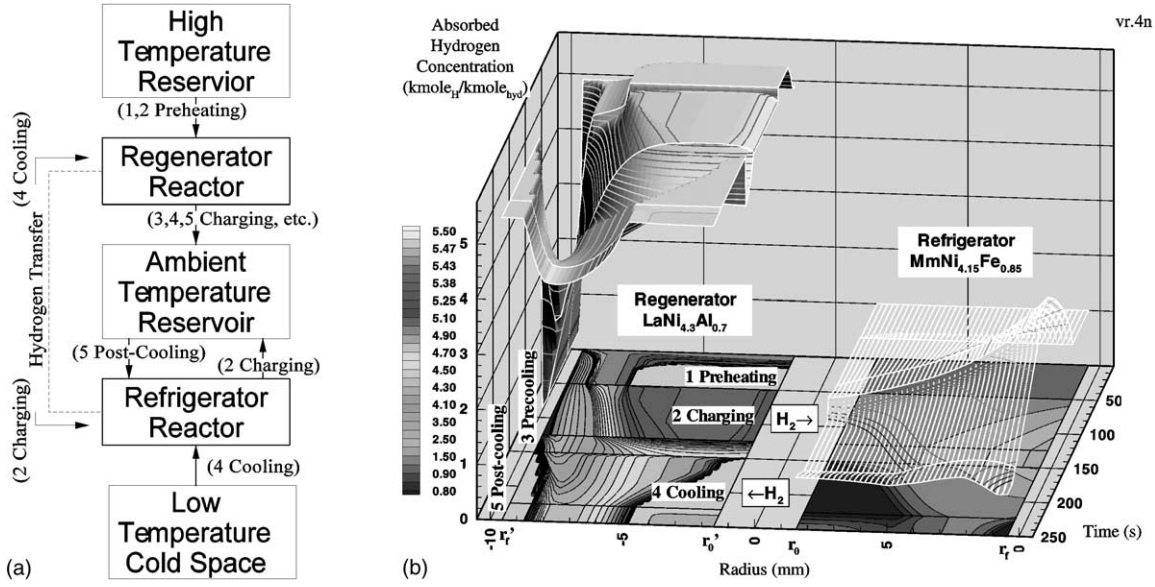

Fig. 1. (a) Block diagram of the heat pump system studied in the paper. Two reactors exchange hydrogen during a cycle of five phases whereby thermal energy is pumped from the low temperature reservoir to the ambient reservoir. Solid lines show heat transfer, (b) LTE simulation of absorbed concentration using a fixed grid, showing the monotonic desorption profile in the regenerator during preheating and charging, and the reaction front during the remaining steps.

purely Lagrangian approach (Crowley, 1967), which is not applicable here. An alternative approach is based upon adjusting the allocation of grid points, and there are two main classes of such methods. In multigridding

or static refinement (Huang and Russell, 1999), features of the solution are identified and a locally refined, but uniform grid, is added. The simplicity of error estimation on uniform grids is retained, but the method is programmatically difficult and appears ill-suited for moving features. In moving grid approaches, on the other hand, the number of elements remains fixed but grid point locations vary with time and are coupled to features in the solution.

In elliptic problems the benefits of iterative adaptive solution procedures falling into the latter category have long been appreciated (Lawal, 1990), and we use this setting to introduce the basic procedure with the convection–diffusion equation,

$$f_{,xx} - v f_{,x} = 0 \quad \text{with} \begin{cases} f(a) = 0, \\ f(b) = 1, \end{cases} \tag{1}$$

where, v is the dimensionless Peclet number and for which the solution is $f(x) = [e^{v(x-a)} - 1][e^{v(b-a)} - 1]^{-1}$, for $v \neq 0$. The solution to Eq. (1) qualitatively resembles the simpler features occurring in the metal hydride system. The procedure is then extended to the time-dependent problem at hand.

We begin with a parameterized coordinate transformation of the independent variables, defined generally as follows:

$$z = z(\xi, \tau), \quad \overset{[0,1]\times[0,\infty]}{\underset{\cap}{z(\xi,\tau)}} \mapsto [a, b] \tag{2}$$

with Jacobian $\mathscr{J} = z_{,\xi}$. Applying the chain rule to Eq. (2), derivatives with respect to the logical space coordinates can be expressed with respect to the physical space coordinates and functions of the Jacobian and the grid speed $z_{,\tau}$ in the following way,

$$\begin{aligned} &\frac{\partial f}{\partial z} = \frac{1}{\mathscr{J}} \frac{\partial f}{\partial \xi}, \quad \frac{\partial^2 f}{\partial z^2} = \frac{1}{\mathscr{J}} \frac{\partial}{\partial \xi}\left(\frac{1}{\mathscr{J}} \frac{\partial f}{\partial \xi}\right), \\ &\frac{\partial f}{\partial t} = \left(\frac{\mathrm{d}t}{\mathrm{d}\tau}\right)^{-1} \left[\frac{\partial f}{\partial \tau} - \frac{1}{\mathscr{J}} \frac{\partial f}{\partial \xi} \frac{\partial z}{\partial \tau}\right]. \end{aligned} \tag{3}$$

Applying Eq. $(3)_{1,2}$ to Eq. (1) results in an equation transformed to logical space coordinates which can then be discretized appropriately.

It is accepted that smoothness is a necessary condition for minimizing truncation error in adaptive schemes (Daripa, 1992; Knupp and Steinberg, 1994). Additional features of any grid scheme must include well posedness and robustness, so that the final grid is not erratically influenced by feature variations, the presence of constraints to prevent grid collapse and excessively small time steps, and the condition that a uniform solution should result in a uniform grid. The smoothness criterion can be ensured by basing the grid distribution upon a Poisson density,

$$z_{,\xi\xi} - \frac{w_{,\xi}}{w} z_{,\xi} = 0 \tag{4}$$

subject to Dirichlet boundary conditions. Eq. (4) arises by setting the grid Jacobian proportional to a weight function, $\mathscr{J} \propto w(z(\xi))$, or $\mathscr{J} \cdot w^{-1} = \text{constant}$. Differentiation by ξ yields Eq. (4); ω^{-1} is sometimes referred to as a monitor function (Bains, 1998). The weight function w controls the local grid point density (Knupp and Steinberg, 1994). A commonly used choice for w which concentrates the mesh in regions of high gradients is $w(z) = (1 + \beta^2 f_{,z}^2)^{-1/2}$ (Mackenzie and Robertson, 2000). Unfortunately, this choice of w can lead to arbitrarily small grid spacing and in practice is overly sensitive to a wide range of spatial scales. A suitable alternative ("`WFGRADLN`"), in which a minimum weight $\mathscr{J}_{\min}$ can be set, is proposed as follows:

$$w = (1 - \mathscr{J}_{\min}) \left[1 + \ln \sqrt{1 + (\beta f_{,z})^2}\right]^{-1} + \mathscr{J}_{\min}, \quad \mathscr{J}_{\min} < 1 \tag{5}$$

The parameter β is related to the characteristic gradient for a problem. This weight function satisfies all the criteria mentioned above. The constant $\mathscr{J}_{\min}$ is chosen to provide the minimum grid Jacobian tolerable. Eq. (4) is solved using the discrete coordinates, resulting in a standard tridiagonal system of nonlinear equations of the form: $\underline{\underline{A}}(\underline{z})\underline{z} = \underline{b}$ which are solved iteratively using LU-decomposition, $\underline{z}^{p+1} = \underline{\underline{A}}^{-1}(\underline{z}^p)\underline{b}$, following the scheme in Fig. 3. An analogous weight function arises by replacing $f_{,z}$ with the curvature $\kappa = f_{,zz}[1 + (\gamma f_{,z})^2]^{-3/2}$ ("`WFKAPPALN`").

Eqs. (1) and (4) were discretized using the difference formulas summarized in Table 1, derived using a null-space technique (many of which, of course, are commonly known). Several pertinent results are summarized in Fig. 2 from which two things can immediately be discerned. First, the maximum truncation error monotonically tracks a decrease in $\mathscr{J}_{\min}$. Secondly, for $J_{\min}$ constant, increased curvature weighting (i.e., $a \to 0$) results in a monotonic decrease in maximum truncation error.

The results apparent in Fig. 2 and from previous experience (Mackenzie and Robertson, 2000; Farrell and Drury, 1998; Daripa, 1992; Bains, 1998; Liu et al., 1998) suggests that reacting flow calculations would benefit from the moving grid approach, and it would seem well suited to the problem at hand. Nevertheless none of the afore-referenced studies involve field source terms, and the behaviour of moving grids applied to such problems has not been adequately investigated. In particular, this class of problems is complicated by the availability of multiple feature variables whose evolution may independently dictate competing grid adaptation. In the sequel this issue is studied through a comparison of a moving grid formulation with benchmark fixed grid results.

Table 1
Finite-difference derivatives on equi-spaced stencils, $O(h^2)$

Derivative	$f^{\llcorner i-4}$	$f^{\llcorner i-3}$	$f^{\llcorner i-2}$	$f^{\llcorner i-1}$	$f^{\llcorner i}$	$f^{\llcorner i+1}$	$f^{\llcorner i+2}$	$f^{\llcorner i+3}$	$f^{\llcorner i+4}$	Leading truncation error
Centered										
$2hf_i'$				-1	0	1				$-\frac{1}{6}h^2f^{(3)}$
h^2f_i''				1	-2	1				$-\frac{1}{12}h^2f^{(4)}$
$2h^3f_i'''$			-1	2	0	-2	1			$-\frac{1}{4}h^2f^{(5)}$
Forward										
$2hf_i'$					-3	4	-1			$\frac{1}{3}h^2f^{(3)}$
h^2f_i''					2	-5	4	-1		$\frac{11}{12}h^2f^{(4)}$
$2h^3f_i'''$					-5	18	-24	14	-3	$\frac{7}{4}f^{(5)}h^2$
$2h^3f_i'''$				-3	10	-12	6	-1		$\frac{1}{4}f^{(5)}h^2$
Backward										
$2hf_i'$			1	-4	3					$\frac{1}{3}h^2f^{(3)}$
h^2f_i''		-1	4	-5	2					$\frac{11}{12}h^2f^{(4)}$
$2h^3f_i'''$	3	-14	24	-18	5					$\frac{7}{4}f^{(5)}h^2$
$2h^3f_i'''$		1	-6	12	-10	3				$\frac{1}{4}h^2f^{(5)}$

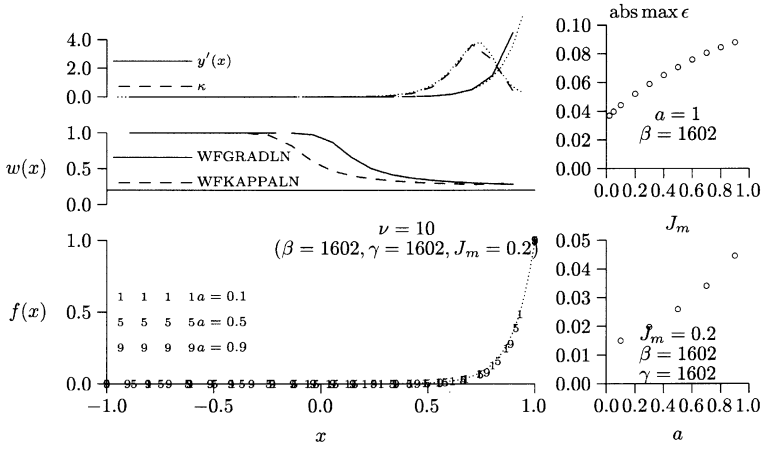

Fig. 2. Adaptive grid test problem. Counter-clockwise from bottom-left: (1) example grids for several values of a, where a is a weighting factor, $w = aw_\nabla + (1-a)w_\kappa$; (2) truncation error behaviour as a function of curvature weighting; (3) truncation error behaviour as a function of minimum Jacobian; (4) comparison of theoretical and estimated gradient and curvature; (5) grid weight fields for $a = 0.7$.

2. Formulation

It is assumed that the system performance and basic reactor dynamics can be modeled by considering the reactors as cylindrical ID domains. The equations (Lloyd et al., 1999) for this formulation are a conservation of mass equation,

$$\left(\frac{K\gamma}{\bar{R}\mu}\right)\left\{p\frac{\partial^2 p}{\partial r^2}+\frac{\partial p}{\partial r}\left[\frac{p}{r}+\frac{\partial p}{\partial r}-\frac{p}{\overset{\mathrm{f}}{T}}\frac{\partial \overset{\mathrm{f}}{T}}{\partial r}\right]\right\}+\dot{\varphi}\overset{\mathrm{f}}{T}$$
$$=\left(\frac{\phi\gamma}{\bar{R}}\right)\left[\frac{\partial p}{\partial t}-\frac{p}{\overset{\mathrm{f}}{T}}\frac{\partial \overset{\mathrm{f}}{T}}{\partial t}\right] \tag{6}$$

a *solid* phase energy equation:

$$(\overset{\mathrm{f}}{T}-\overset{\mathrm{s}}{T})h_{\mathrm{sf}}\frac{\mathrm{d}A_{\mathrm{sf}}}{\mathrm{d}V_{(\mathrm{c})}}+(1-\phi)k_{\mathrm{s}}\left[\frac{1}{r}\frac{\partial \overset{\mathrm{s}}{T}}{\partial r}+\frac{\partial^2 \overset{\mathrm{s}}{T}}{\partial r^2}\right]+g$$
$$-c_{\mathrm{p_f}}\dot{\varphi}\begin{cases}0, & \dot{\varphi}>0,\ \text{desorp.}\\ \overset{\mathrm{f}}{T}-\overset{\mathrm{s}}{T}, & \dot{\varphi}<0,\ \text{adsorp.}\end{cases}$$
$$=(1-\phi)\rho_{\mathrm{s}}c_{\mathrm{v_s}}\frac{\partial \overset{\mathrm{s}}{T}}{\partial t}\quad (\mathrm{W/m^3_{(c)}}) \tag{7}$$

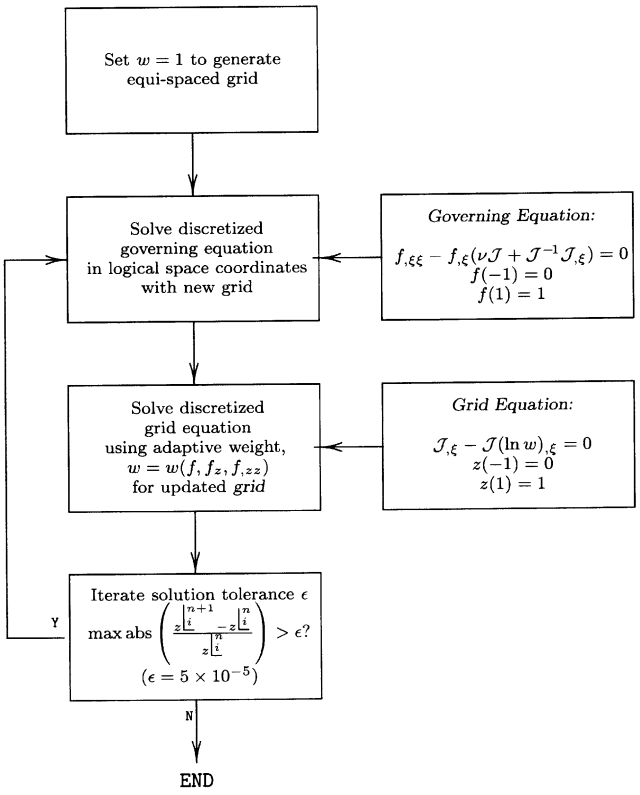

Fig. 3. Flowchart of the adaptive grid procedure used for both time-independent and dependent problems.

and a *fluid* phase energy equation:

$$
\begin{aligned}
&(\overset{\mathrm{s}}{T} - \overset{\mathrm{f}}{T})h_{\mathrm{sf}}\frac{\mathrm{d}A_{\mathrm{sf}}}{\mathrm{d}V_{(\mathrm{c})}} + \phi k_{\mathrm{f}}\left[\frac{1}{r}\frac{\partial \overset{\mathrm{f}}{T}}{\partial r} + \frac{\partial^2 \overset{\mathrm{f}}{T}}{\partial r^2}\right] \\
&\quad + \frac{c_{\mathrm{p_f}}\gamma K}{\bar{R}\mu}\left[\frac{p}{r}\frac{\partial p}{\partial r} + \left(\frac{\partial p}{\partial r}\right)^2 + p\frac{\partial^2 p}{\partial r^2}\right] \\
&\quad + c_{\mathrm{p_f}}\dot{\varphi}\begin{cases} \overset{\mathrm{s}}{T} - \overset{\mathrm{f}}{T}, & \dot{\varphi} > 0, \text{desorp.} \\ 0, & \dot{\varphi} < 0, \text{adsorp.} \end{cases} \\
&\quad = \left(\frac{\phi c_{\mathrm{v_f}}\gamma}{\bar{R}}\right)\frac{\partial p}{\partial t} \quad (\mathrm{W/m^3_{(c)}}).
\end{aligned} \tag{8}
$$

Hydrogen is assumed to be an ideal gas. The source terms g and $\dot{\varphi}$ in these equations are given by the following (Lloyd et al., 1998):

$$
\begin{aligned}
\dot{\varphi} &= -\frac{1}{2}N_0\left(\frac{\partial x}{\partial t}\right)_r \gamma H_2 \wp \quad \left(\frac{\mathrm{kg_{H_2}}}{\mathrm{s\,m^3}}\right), \\
g &= \frac{1}{2}N_0\left(\frac{\partial x}{\partial t}\right)_r |\Delta H| \wp \quad \left(\frac{\mathrm{J}}{\mathrm{s\,m^3}}\right).
\end{aligned} \tag{9}
$$

The local reaction rate in Eq. (9) is an Arrhenius type, at *constant radius*, i.e.,

$$
\left(\frac{\partial x}{\partial t}\right)_r = A\mathrm{e}^{-E_{\mathrm{a}}/\bar{R}T}\ln\left(\frac{p}{p_{\mathrm{eq}}}\right) \quad \left(\frac{\mathrm{kmol_{H_2}}}{\mathrm{s\,particle_h}}\right). \tag{10}
$$

A reasonable estimate for $\mathrm{d}A_{\mathrm{sf}}/\mathrm{d}V_{(\mathrm{c})} \sim \pi/2r$; assuming spherical particles with $r = 15$ μm gives $\mathrm{d}A_{\mathrm{sf}}/\mathrm{d}V_{(\mathrm{c})} \approx 10^5$ ($\mathrm{m^2/m^3_{(c)}}$). Values for cohesive materials (sintered spherical copper powders) are reported to depend quite sensitively on porosity, densification history, applied tractions, internal stress history, and other factors (Reid and Oakberg, 1990). Somewhat arbitrarily a value of $\mathrm{d}A_{\mathrm{sf}}/\mathrm{d}V = 10^4$ ($\mathrm{m^2/m^3_{(c)}}$) was used as a baseline. A standard correlation for h_{sf} (for spherical particles) is available (Kaviany, 1995, p. 403):

$$
Nu_{\mathrm{D}} = \frac{h_{\mathrm{sf}}D}{k_{\mathrm{f}}} = 2 + 1.1\,Re_{\mathrm{D}}^{0.6}\,Pr^{1/3} \tag{11}
$$

Fukuda et al. (1992) derive a similar relationship $Nu = f(Re)$ for a larger class of porous materials. In any case, the contribution from the second term is ignored in this work due to the small values of Re_{D} (or $Re_{\sqrt{\mathrm{K}}}$) (Lloyd et al., 1995). A reasonable range of values to examine is thus $h_{\mathrm{sf}} \in [10^2, 10^3]$. In the calculations reported here, a value of $h_{\mathrm{sf}} = 1000$ ($\mathrm{W/m^3\,K}$) was used, in conjunction with $k_{\mathrm{f}} = 10^{-1}$ ($\mathrm{W/m\,K}$).

3. Boundary conditions

The boundary conditions for a NLTE formulation are summarized from Lloyd et al. (1999). First, it is assumed that the sensible energy resulting from transpiration from one reactor and injection into the other is deposited within a macroscopically thin boundary layer on the injection side, as depicted in Fig. 4a (White, 1991). This implies that the transport of sensible heat can be represented as a boundary heat flux between fluid phases. This avoids the problem of introducing a "boundary" surface convection coefficient, as used in Dang and Delcambre (1987).

Secondly, the degree to which energy is transferred between the incoming phase and the resident phases can be expected to depend upon a characteristic time which is a function of the injection velocity and the resident matrix constituents and their thermodynamic state. For sintered porous metal compacts it is reasonable to conjecture that the boundary energy transfer is dominated by processes confined within a microscopically significant entrance depth δr ("assumption two"). A value of $\delta r = 0.1$ (mm) was used, corresponding roughly to 3–5 times the characteristic diameter of the starting powder size. This assumption implies that interphase energy transport can be modeled as a solid-phase heat flux boundary condition. These two assumptions can be written as follows:

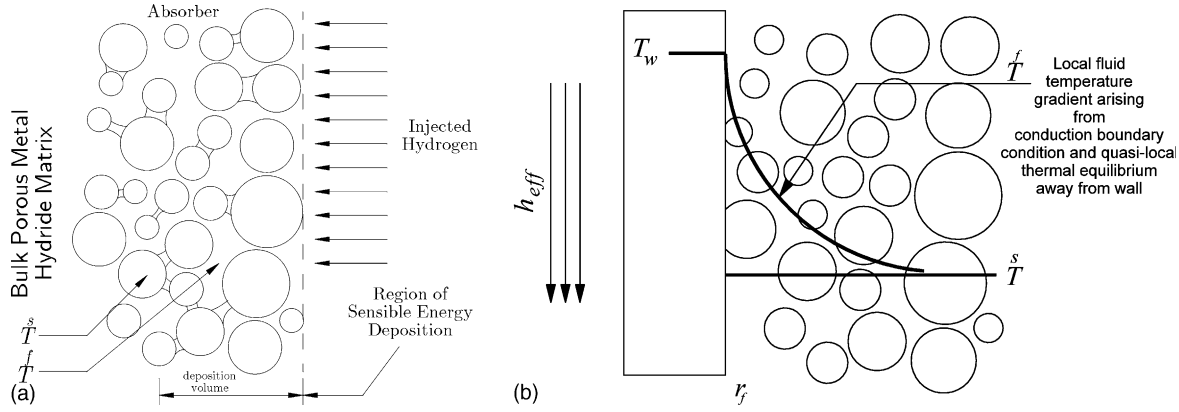

Fig. 4. (a) Boundary region at $r_{0'}$, t. Hydrogen at $\overset{\mathrm{f}}{T}(r_0,t)$ is injected into the reactor with interface phase temperatures $\overset{\mathrm{f}}{T}(r_{0'},t)$ and $\overset{\mathrm{s}}{T}(r_{0'},t)$. (b) Schematic diagram of conditions existing at the microscopic level dictating idealizations made for interface boundary conditions.

$$\underbrace{-(c_{\mathrm{p_f}}\rho_{\mathrm{f}}v_{\mathrm{f}})\left[\overset{\mathrm{f}}{T}(r_0,t)-\overset{\mathrm{f}}{T}(r_{0'},t)\right]A_0}_{\substack{\text{equivalent energy transport}\\ \text{from the refrigerator fluid phase}\\ \text{to the regenerator fluid phase}}}\quad(\mathrm{J/s})$$

$$=-k_{f'}\frac{\partial\overset{\mathrm{f}}{T}(r_{0'},t)}{\partial r}A_{0'} \tag{12a}$$

$$\underbrace{h_{\mathrm{sf}'}\frac{\mathrm{d}A_{\mathrm{sf}'}}{\mathrm{d}V_{(\mathrm{c})'}}\left[\overset{\mathrm{f}}{T}(r_{0'},t)-\overset{\mathrm{s}}{T}(r_{0'}t)\right]V_{0'}}_{\substack{\text{energy transport between phases}\\ \text{in the boundary deposition region}}}\quad(\mathrm{J/s})$$

$$=-k_{s'}\frac{\partial\overset{\mathrm{s}}{T}(r_{0'},t)}{\partial r}A_{0'}. \tag{12b}$$

In Eq. (12b) $V_{0'}=\pi[(r_{0'}+\delta r)^2-r_{0'}^2]L'$ denotes the deposition volume. Eqs. (12a) and (12b) uses nomenclature consistent for transpiration *from* the refrigerator *to* the regenerator. Eqs. (12a) and (12b) apply to the regenerator.

The remaining two boundary conditions for the transpiring refrigerator are constraints on the phase temperature gradients—i.e., the adiabatic approximations,

$$\frac{\partial\overset{\mathrm{s}}{T}(r_0,t)}{\partial r}=0, \tag{13a}$$

$$\frac{\partial\overset{\mathrm{f}}{T}(r_0,t)}{\partial r}=0 \tag{13b}$$

since there is no thermal connection of the boundary to the regenerator. In addition, when the reactors are coupled the mechanical driving potential must be equal:

$$p(r_{0'},t)=p(r_0,t). \tag{14}$$

Finally, the following steady-state mass flow condition must be satisfied,

$$\left(\frac{K'}{K}\right)\frac{1}{T(r_{0'},t)}\frac{\partial p(r_{0'},t)}{\partial r}\frac{A_{0'}}{A_0}=-\frac{1}{T(r_0,t)}\frac{\partial p(r_0,t)}{\partial r}. \tag{15}$$

There are six unknowns: p, p', $\overset{\mathrm{f}}{T}$, $\overset{\mathrm{f}}{T'}$, $\overset{\mathrm{s}}{T}$ and $\overset{\mathrm{s}}{T'}$. Eqs. (12a)–(15) provide the required boundary conditions at the core boundaries.

Fig. 4b depicts the temperature gradients expected to exist in the local region of the reactor-wall boundary.

The physical picture must be modified to include heat transfer between a solid–fluid matrix and the single solid boundary (with the associated temperature T_{w}). In a one-dimensional geometry there is no tangential component to the hydrogen motion. Therefore, heat transfer between the wall and fluid phase must occur entirely through conduction,

$$T_{\mathrm{w}}(t)=\overset{\mathrm{f}}{T}(r_{\mathrm{c}},t). \tag{16}$$

The gradient of the solid-phase temperature is postulated to depend upon a solid–solid contact conductance, $h_{\mathrm{c_{sw}}}$:

$$-k_{\mathrm{s}}\frac{\partial\overset{\mathrm{s}}{T}(r_{\mathrm{c}},t)}{\partial r}(1-\phi)A_{\mathrm{c}}=h_{\mathrm{c_{sw}}}[\overset{\mathrm{s}}{T}(r_{\mathrm{c}},t)-T_{\mathrm{w}}(t)](1-\phi)A_{\mathrm{c}} \tag{17}$$

Eqs. (16) and (17) are reasonable approximations for the macroscopic boundary conditions.

Numerical difficulties are introduced, however, by Eq. (16). Near the boundary, the use of a single, spatially homogeneous wall temperature in Eq. (16) implies the existence of a large temperature gradient in the fluid phase due to the condition $\overset{\mathrm{f}}{T}\to\overset{\mathrm{s}}{T}$, as shown in Fig. 4b. For the most part, the gradients are also confined in time. For this reason, and because of the low thermal conductivity of hydrogen, the gradient of the fluid phase temperature was approximated using the same form as Eq. (17):

$$-k_{\mathrm{f}}\frac{\partial \overset{\mathrm{f}}{T}(r_{\mathrm{c}},t)}{\partial r}\phi A_{\mathrm{c}} = h_{\mathrm{c_{fw}}}[\overset{\mathrm{f}}{T}(r_{\mathrm{c}},t) - T_{\mathrm{w}}(t)]\phi A_{\mathrm{c}} \tag{18}$$

A value of $h_{\mathrm{c_{fw}}} = 50$ (W/m^2 K) was used. This value eliminated the numerical instabilities referred to earlier. Eqs. (17) and (18) are the wall boundary conditions for the NLTE model, in conjunction with the following energy balance on the reactor wall:

$$\begin{aligned}\frac{\mathrm{d}(c_{\mathrm{w}}\rho_{\mathrm{w}}V_{\mathrm{w}}T_{\mathrm{w}})}{\mathrm{d}t} &= h_{\mathrm{c_{sw}}}[\overset{\mathrm{s}}{T}(r_{\mathrm{c}},t) - T_{\mathrm{w}}(t)](1-\phi)A_{\mathrm{c}} \\ &\quad + h_{\mathrm{c_{sf}}}[\overset{\mathrm{f}}{T}(r_{\mathrm{c}},t) - T_{\mathrm{w}}(t)]\phi A_{\mathrm{c}} \\ &\quad - \underbrace{h_{\infty}A_{\mathrm{f}}(T_{\mathrm{w}}(t) - T_{res})}_{\substack{\text{heat transfer from}\\ \text{reactor wall}\\ \text{into external thermal reservoir}}}\end{aligned} \tag{19}$$

The first two terms describe heat transfer from the two-phase reactor matrix into reactor wall. The last term describes heat transfer from the reactor wall into the external thermal reservoir.

4. Logical space coordinates

By substituting Eq. (3) into the physical space governing equations, the transformed equations become:

$$\begin{aligned}&\left(\frac{K\gamma}{\bar{R}\mu}\right)\left\{p\left[-\frac{1}{\mathscr{J}^3}\frac{\partial \mathscr{J}}{\partial\xi}\frac{\partial p}{\partial\xi}+\frac{1}{\mathscr{J}^2}\frac{\partial^2 p}{\partial\xi^2}\right]\right. \\ &\left.+\frac{1}{\mathscr{J}}\frac{\partial p}{\partial\xi}\left[\frac{p}{r(\xi)}+\frac{1}{\mathscr{J}}\frac{\partial p}{\partial\xi}-\frac{p}{\overset{\mathrm{f}}{T}}\frac{1}{\mathscr{J}}\frac{\partial \overset{\mathrm{f}}{T}}{\partial\xi}\right]\right\}+\dot{\phi}\overset{\mathrm{f}}{T} \\ &=\left(\frac{\phi\gamma}{\bar{R}}\right)\left\{\left(\frac{\mathrm{d}t}{\mathrm{d}\tau}\right)^{-1}\left[\frac{\partial p}{\partial\tau}-\frac{1}{\mathscr{J}}\frac{\partial p}{\partial\xi}\frac{\partial r}{\partial\tau}\right]\right. \\ &\left.-\frac{p}{\overset{\mathrm{f}}{T}}\left(\frac{\mathrm{d}t}{\mathrm{d}\tau}\right)^{-1}\left[\frac{\partial \overset{\mathrm{f}}{T}}{\partial\tau}-\frac{1}{\mathscr{J}}\frac{\partial \overset{\mathrm{f}}{T}}{\partial\xi}\frac{\partial r}{\partial\tau}\right]\right\}\end{aligned} \tag{20}$$

$$\begin{aligned}&(\overset{\mathrm{f}}{T}-\overset{\mathrm{s}}{T})h_{\mathrm{sf}}\frac{\mathrm{d}A_{\mathrm{sf}}}{\mathrm{d}V_{(\mathrm{c})}}+(1-\phi)k_{\mathrm{s}}\left[\frac{1}{r(\xi)}\frac{1}{\mathscr{J}}\frac{\partial \overset{\mathrm{s}}{T}}{\partial\xi}\right. \\ &\left.+\frac{1}{\mathscr{J}}\frac{\partial}{\partial\xi}\left(\frac{1}{\mathscr{J}}\frac{\partial \overset{\mathrm{s}}{T}}{\partial\xi}\right)\right]+g \\ &-c_{\mathrm{p_f}}\dot{\phi}\begin{cases}0, & \dot{\phi}>0,\text{desorp.}\\ \overset{\mathrm{f}}{T}-\overset{\mathrm{s}}{T}, & \dot{\phi}<0,\text{adsorp.}\end{cases} \\ &=(1-\phi)\rho_{\mathrm{s}}c_{\mathrm{v_s}}\left(\frac{\mathrm{d}t}{\mathrm{d}\tau}\right)^{-1}\left[\frac{\partial \overset{\mathrm{s}}{T}}{\partial\tau}-\frac{1}{\mathscr{J}}\frac{\partial \overset{\mathrm{s}}{T}}{\partial\xi}\frac{\partial r}{\partial\tau}\right]\quad(\mathrm{W/m^3_{(c)}})\end{aligned} \tag{21}$$

$$\begin{aligned}&(\overset{\mathrm{s}}{T}-\overset{\mathrm{f}}{T})h_{\mathrm{sf}}\frac{\mathrm{d}A_{\mathrm{sf}}}{\mathrm{d}V_{(\mathrm{c})}}+\phi k_{\mathrm{f}}\left[\frac{1}{r(\xi)}\frac{1}{\mathscr{J}}\frac{\partial \overset{\mathrm{f}}{T}}{\partial\xi}\right. \\ &\left.+\frac{1}{\mathscr{J}}\frac{\partial}{\partial\xi}\left(\frac{1}{\mathscr{J}}\frac{\partial \overset{\mathrm{f}}{T}}{\partial\xi}\right)\right]+\frac{c_{\mathrm{p_f}}\gamma K}{\bar{R}\mu}\left[\frac{p}{r(\xi)}\frac{1}{\mathscr{J}}\frac{\partial p}{\partial\xi}\right. \\ &\left.+\left(\frac{1}{\mathscr{J}}\frac{\partial p}{\partial\xi}\right)^2+p\frac{1}{\mathscr{J}}\frac{\partial}{\partial\xi}\left(\frac{1}{\mathscr{J}}\frac{\partial p}{\partial\xi}\right)\right] \\ &+c_{\mathrm{p_f}}\dot{\phi}\begin{cases}\overset{\mathrm{s}}{T}-\overset{\mathrm{f}}{T}, & \dot{\phi}>0,\text{desorp.}\\ 0, & \dot{\phi}>0,\text{adsorp.}\end{cases} \\ &=\left(\frac{\phi c_{\mathrm{v_f}}\gamma}{\bar{R}}\right)\left(\frac{\mathrm{d}t}{\mathrm{d}\tau}\right)^{-1}\left[\frac{\partial p}{\partial\tau}-\frac{1}{\mathscr{J}}\frac{\partial p}{\partial\xi}\frac{\partial r}{\partial\tau}\right]\quad(\mathrm{W/m^3_{(c)}})\end{aligned} \tag{22}$$

The independent spatial variable is understood to be ξ in these equations. The discretizations of Eqs. (6)–(8) using an explicit scheme were given in detail in (Lloyd et al., 1999). Under the transformation $r \mapsto \xi$ the structure of these equations remains unchanged. As a result, the difference method can be applied unchanged to Eqs. (20)–(22) and the boundary conditions.

5. Discretization

A formal discretization is used, as shown in Fig. 5. Pressure, temperatures and concentration are node centered. Velocities are derived from the pressure gradient, and are not calculated independently. With the notation $f\big|_{\underline{i}}^{n}$ denoting the value of the function f at the logical node i at the logical time step n, the solid-phase energy equation, Eq. (21), becomes:

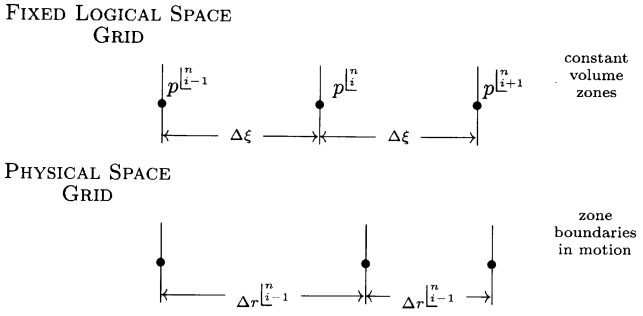

Fig. 5. Grid nomenclature. The physical cell volume is related to the computational cell volume by $V = \mathscr{J}V_0$.

$$
\begin{aligned}
{}^{\mathrm{s}}T_i^{n+1} &= {}^{\mathrm{s}}T_i^n + r_\tau \Delta\tau (\mathscr{J}_i^n)^{-1} {}^{\mathrm{s}}T_{,\xi}{}_i^n \\
&\quad + \Delta\tau\Lambda \frac{h_{\mathrm{sf}} \mathrm{d}A_{\mathrm{sf}}/\mathrm{d}V_{(c)}}{(1-\phi)\rho_{\mathrm{s}} c_{\mathrm{v_s}}} ({}^{\mathrm{f}}T_i^n - {}^{\mathrm{s}}T_i^n) \\
&\quad + \Delta\tau\Lambda \frac{k_{\mathrm{s}}}{\rho_{\mathrm{s}} c_{\mathrm{v_s}}} \left[\frac{1}{r_i^n} (\mathscr{J}_i^n)^{-1} {}^{\mathrm{s}}T_{,\xi}{}_i^n \right. \\
&\quad \left. + {}^{\mathrm{s}}T_{,\xi\xi}{}_i^n (\mathscr{J}_i^n)^{-2} - {}^{\mathrm{s}}T_{,\xi}{}_i^n (\mathscr{J}_i^n)^{-3} \mathscr{J}_{,\xi}{}_i^n \right] \\
&\quad + \Delta\tau\Lambda \frac{g}{(1-\phi)\rho_{\mathrm{s}} c_{\mathrm{v_s}}} \\
&\quad - \Delta\tau\Lambda \frac{c_{\mathrm{p_f}}}{(1-\phi)\rho_{\mathrm{s}} c_{\mathrm{v_s}}} \dot{\phi} \begin{cases} 0, \\ {}^{\mathrm{f}}T_i^n - {}^{\mathrm{s}}T_i^n. \end{cases}
\end{aligned} \tag{23}
$$

Similarly, the discretization of the fluid-phase energy equation Eq. (22) leads to,

$$
\begin{aligned}
p_i^{n+1} &= p_i^n + r_\tau \Delta\tau (\mathscr{J}_i^n)^{-1} p_{,\xi}{}_i^n \\
&\quad + \Delta\tau\Lambda \left(\frac{\bar{R}}{\phi c_{\mathrm{v_f}} \gamma} \right) h_{\mathrm{sf}} \frac{\mathrm{d}A_{\mathrm{sf}}}{\mathrm{d}V_{(c)}} ({}^{\mathrm{s}}T_i^n - {}^{\mathrm{f}}T_i^n) \\
&\quad + \Delta\tau\Lambda \left(\frac{k_f \bar{R}}{c_{\mathrm{v_f}} \gamma} \right) \left[\frac{1}{r_i^n} (\mathscr{J}_i^n)^{-1} {}^{\mathrm{f}}T_{,\xi}{}_i^n \right. \\
&\quad \left. + (\mathscr{J}_i^n)^{-2} {}^{\mathrm{f}}T_{,\xi\xi}{}_i^n - (\mathscr{J}_i^n)^{-3} \mathscr{J}_{,\xi}{}_i^n {}^{\mathrm{f}}T_{,\xi}{}_i^n \right] \\
&\quad + \Delta\tau\Lambda \left(\frac{K c_{\mathrm{p_f}}}{\phi\mu c_{\mathrm{v_f}}} \right) \left[\frac{p_i^n}{r_i^n} (\mathscr{J}_i^n)^{-1} p_{,\xi}{}_i^n + (\mathscr{J}_i^n)^{-2} (p_{,\xi}{}_i^n)^2 \right. \\
&\quad \left. + p_i^n (\mathscr{J}_i^n)^{-2} p_{,\xi\xi}{}_i^n - p_i^n (\mathscr{J}_i^n)^{-3} \mathscr{J}_{,\xi}{}_i^n p_{,\xi}{}_i^n \right] \\
&\quad + \Delta\tau\Lambda \left(\frac{\bar{R} c_{\mathrm{p_f}}}{\phi\gamma c_{\mathrm{v_f}}} \right) \dot{\phi} \begin{cases} {}^{\mathrm{s}}T_i^n - {}^{\mathrm{f}}T_i^n \\ 0 \end{cases}
\end{aligned} \tag{24}
$$

Finally, the conservation of mass equation becomes:

$$
\begin{aligned}
&p_i^{n+1} - \frac{p_i^n}{{}^{\mathrm{f}}T_i^n} {}^{\mathrm{f}}T_i^{n+1} \\
&\quad = \Delta\tau \frac{r_\tau}{\mathscr{J}} \left[p_{,\xi}{}_i^n - p_i^n {}^{\mathrm{f}}T_{,\xi}{}_i^n \Big/ {}^{\mathrm{f}}T_i^n \right] + \dot{\phi} {}^{\mathrm{f}}T \frac{\Lambda \Delta\tau \bar{R}}{\phi\gamma} \\
&\qquad + \frac{\Lambda \Delta\tau K}{\phi\mu} \left[\frac{p}{\mathscr{J}^2} p_{,\xi\xi}{}_i^n - \frac{p}{\mathscr{J}^3} \mathscr{J}_{,\xi} p_{,\xi}{}_i^n + \frac{1}{\mathscr{J}} \frac{p}{r(\xi)} p_{,\xi}{}_i^n \right. \\
&\qquad \left. + \frac{1}{\mathscr{J}^2} (p_{,\xi}{}_i^n)^2 - \frac{p}{\mathscr{J}^2} \frac{1}{{}^{\mathrm{f}}T} {}^{\mathrm{f}}T_{,\xi}{}_i^n p_{,\xi}{}_i^n \right]
\end{aligned} \tag{25}
$$

Eqs. (23) and (24) may be solved directly for ${}^{\mathrm{s}}T_i^{n+1}$ and p_i^{n+1}; Eq. (25) provides ${}^{\mathrm{f}}T_i^{n+1}$. The discretization can be shown by standard methods to be consistent (Lloyd, 1998) and second-order accurate overall (Strikwerda, 1989).

The proper representation of the source terms from Eq. (9) follows from Eq. (3):

$$
\left(\frac{\partial x}{\partial t} \right)_r = \left(\frac{\mathrm{d}t}{\mathrm{d}\tau} \right)^{-1} \left[\left(\frac{\partial x}{\partial \tau} \right)_\xi - \frac{1}{\mathscr{J}} \left(\frac{\partial x}{\partial \xi} \right)_\tau r_\tau \right], \tag{26}
$$

where the intrinsic grid reaction rate (the local rate at the location $\xi = \xi_0$ moving with grid speed $r_\tau(\xi_0)$) is the following modification of Eq. (10):

$$
\left(\frac{\partial x}{\partial \tau} \right)_\xi = A \mathrm{e}^{-E_{\mathrm{a}}/\bar{R}T} \ln \left(\frac{p}{p_{\mathrm{eq}}} \right) \quad \left(\frac{\mathrm{kmol_{H_2}}}{\mathrm{s\,particle_h}} \right) \tag{27}
$$

Eq. (27) is integrated at each timestep by an Euler integrator:

$$
\frac{x_i^{n+1} - x_i^n}{\Delta\tau} = A \mathrm{e}^{-E_{\mathrm{a}}/\bar{R}T_i^n} \ln \left(\frac{p_i^n}{p_{\mathrm{eq}}{}_i^n} \right). \tag{28}
$$

The boundary conditions are discretized as follows. Eqs. (13a) and (13b) are uncoupled and discretized using second-order difference expressions:

$$
{}^{\mathrm{s}}T_1^n = \tfrac{4}{3} {}^{\mathrm{s}}T_2^n - \tfrac{1}{3} {}^{\mathrm{s}}T_3^n = a_4, \quad {}^{\mathrm{f}}T_1^n = \tfrac{4}{3} {}^{\mathrm{f}}T_2^n - \tfrac{1}{3} {}^{\mathrm{f}}T_3^n = a_5 \tag{29}
$$

and from Eq. (14), $p_1^n = p_{1'}^n$. The discretized steady-state mass flow conditions, Eq. (15), is,

$$
\begin{aligned}
&\left(\frac{K'}{K} \right) \frac{1}{\mathscr{J}_{1'}^n} \frac{1}{{}^{\mathrm{f}}T_{1'}^n} \frac{4p_{2'}^n - p_{3'}^n - 3\boxed{p_{1'}^n}}{2\Delta\xi'} \frac{A_{0'}}{A_0} \\
&\quad = \frac{1}{{}^{\mathrm{f}}T_1^n} \frac{1}{\mathscr{J}_1^n} \frac{4p_2^n - p_3^n - 3p_1^n}{2\Delta\xi}.
\end{aligned} \tag{30}
$$

Solving for $p_{1'}^n$ (the boxed term in Eq. (30)) gives,

$$
\begin{aligned}
p_{1'}^n &= \tfrac{1}{3} \left(4p_2^n - p_3^n - 3p_1^n \right) \left[\frac{\Delta\xi'}{\Delta\xi} \frac{\mathscr{J}_{1'}^n}{\mathscr{J}_1^n} \frac{A_0 K {}^{\mathrm{f}}T_{1'}^n}{A_{0'} K' {}^{\mathrm{f}}T_1^n} \right] \\
&\quad + \tfrac{4}{3} p_{2'}^n - \tfrac{1}{3} p_{3'}^n.
\end{aligned} \tag{31}
$$

But from Eqs. (31) and (29), $p_1^n = p_{1'}^n$,

$$
p_1^n = p_{1'}^n = \frac{a_3 a_5 + a_1 a_2 {}^{\mathrm{f}}T_{1'}^n}{a_5 + a_1 {}^{\mathrm{f}}T_{1'}^n}, \tag{32}
$$

where $a_1 = \Delta\xi' A_0 K \mathscr{J}_{1'}^n / \Delta\xi A_{0'} K' \mathscr{J}_1^n$, $a_2 = \frac{4}{3} p_2^n - \frac{1}{3} p_3^n$, and $a_3 = \frac{4}{3} p_{2'}^n - \frac{1}{3} p_{3'}^n$. The solid-phase energy boundary conditions, Eq. (12b), is discretized as follows:

$$
\begin{aligned}
&-k_{s'} \frac{1}{\mathscr{J}_{1'}^n} \frac{4 {}^{\mathrm{s}}T_{2'}^n - {}^{\mathrm{s}}T_{3'}^n - 3\boxed{{}^{\mathrm{s}}T_{1'}^n}}{2\Delta\xi'} A_{0'} \\
&\quad = h_{\mathrm{sf}'} \frac{\mathrm{d}A_{\mathrm{sf}'}}{\mathrm{d}V_{(c)'}} \left[{}^{\mathrm{f}}T_{1'}^n - \boxed{{}^{\mathrm{s}}T_{1'}^n} \right] V_{0'}
\end{aligned} \tag{33}
$$

or

$$
{}^{\mathrm{s}}T_{1'}^n = \frac{b_1 {}^{\mathrm{f}}T_{1'}^n + b_2}{1 + b_1}, \tag{34}
$$

where

$$
b_1 = h_{\mathrm{sf}'} (\mathrm{d}A_{\mathrm{sf}'}/\mathrm{d}V_{(c)'}) ((2\Delta\xi' V_{0'} \mathscr{J}_{1'}^n)/(3k_{s'} A_{0'}))
$$

and

$$b_2 = \tfrac{4}{3}\overset{\mathrm{s}}{T}{}^{\lfloor n}_{\lfloor 2'} - \tfrac{1}{3}\overset{\mathrm{s}}{T}{}^{\lfloor n}_{\lfloor 3'}.$$

The fluid-phase energy coupling boundary condition, Eq. (12a), takes the following form:

$$\begin{aligned} &- k_{f'}\frac{1}{\mathscr{J}^{\lfloor n}_{\lfloor 1'}}\frac{4\overset{\mathrm{f}}{T}{}^{\lfloor n}_{\lfloor 2'} - \overset{\mathrm{f}}{T}{}^{\lfloor n}_{\lfloor 3'} - 3\boxed{\overset{\mathrm{f}}{T}{}^{\lfloor n}_{\lfloor 1'}}}{2\Delta\xi'} \\ &= \frac{A_0 c_{\mathrm{p_f}}\gamma K}{A_{0'}\bar{R}\mu}\frac{p^{\lfloor n}_{\lfloor 1}}{\overset{\mathrm{f}}{T}{}^{\lfloor n}_{\lfloor 1}}\frac{1}{\mathscr{J}^{\lfloor n}_{\lfloor 1}}\frac{4p^{\lfloor n}_{\lfloor 2} - p^{\lfloor n}_{\lfloor 3} - 3p^{\lfloor n}_{\lfloor 1}}{2\Delta\xi}\left[\overset{\mathrm{f}}{T}{}^{\lfloor n}_{\lfloor 1} - \boxed{\overset{\mathrm{f}}{T}{}^{\lfloor n}_{\lfloor 1'}}\right]a_7 - \overset{\mathrm{f}}{T}{}^{\lfloor n}_{\lfloor 1'} \\ &= \frac{a_6}{a_5}p^{\lfloor n}_{\lfloor 1}\left(a_2 - p^{\lfloor n}_{\lfloor 1}\right)\left(a_5 - \overset{\mathrm{f}}{T}{}^{\lfloor n}_{\lfloor 1'}\right), \end{aligned} \tag{35}$$

where

$$a_6 = -(\Delta\xi'/\Delta\xi)(A_0/A_{0'})((c_{\mathrm{p_f}}\gamma K\mathscr{J}^{\lfloor n}_{\lfloor 1'})/(\bar{R}\mu k_{f'}\mathscr{J}^{\lfloor n}_{\lfloor 1}))$$

and

$$a_7 = \tfrac{4}{3}\overset{\mathrm{f}}{T}{}^{\lfloor n}_{\lfloor 2'} - \tfrac{1}{3}\overset{\mathrm{f}}{T}{}^{\lfloor n}_{\lfloor 3'}$$

Eq. (35) may be expressed in terms of $\overset{\mathrm{f}}{T}{}^{\lfloor n}_{\lfloor 1'}$ by substituting in Eq. (32) for $p^{\lfloor n}_{\lfloor 1}$:

$$\begin{aligned} a_7 - \overset{\mathrm{f}}{T}{}^{\lfloor n}_{\lfloor 1'} = {} & \overbrace{(a_1a_2a_3 - a_1a_2^2)a_6}^{A}\,\overset{\mathrm{f}}{T}{}^{\lfloor n2}_{\lfloor 1'} \\ & + \overbrace{(a_3^2 - (1+a_1)a_2a_3 + a_1a_2^2)a_5a_6}^{B}\,\overset{\mathrm{f}}{T}{}^{\lfloor n}_{\lfloor 1'} \\ & + \overbrace{(a_2a_3 - a_3^2)a_5^2a_6}^{C}/a_1^2\overset{\mathrm{f}}{T}{}^{\lfloor n2}_{\lfloor 1'} + 2a_1a_5\overset{\mathrm{f}}{T}{}^{\lfloor n}_{\lfloor 1'} + a_5^2 \end{aligned}$$

$$a_7 - \overset{\mathrm{f}}{T}{}^{\lfloor n}_{\lfloor 1'} = \frac{A\overset{\mathrm{f}}{T}{}^{\lfloor n2}_{\lfloor 1'} + B\overset{\mathrm{f}}{T}{}^{\lfloor n}_{\lfloor 1'} + C}{a_1^2\overset{\mathrm{f}}{T}{}^{\lfloor n2}_{\lfloor 1'} + 2a_1a_5\overset{\mathrm{f}}{T}{}^{\lfloor n}_{\lfloor 1'} + a_5^2} \tag{36}$$

or

$$\begin{aligned} & a_7(a_1^2\overset{\mathrm{f}}{T}{}^{\lfloor n2}_{\lfloor 1'} + 2a_1a_5\overset{\mathrm{f}}{T}{}^{\lfloor n}_{\lfloor 1'} + a_5^2) - a_1^2\overset{\mathrm{f}}{T}{}^{\lfloor n3}_{\lfloor 1'} - 2a_1a_5\overset{\mathrm{f}}{T}{}^{\lfloor n2}_{\lfloor 1'} - a_5^2\overset{\mathrm{f}}{T}{}^{\lfloor n}_{\lfloor 1'} \\ & \quad = A\overset{\mathrm{f}}{T}{}^{\lfloor n2}_{\lfloor 1'} + B\overset{\mathrm{f}}{T}{}^{\lfloor n}_{\lfloor 1'} + C, \\ & \overbrace{-a_1^2}^{D}\,\overset{\mathrm{f}}{T}{}^{\lfloor n3}_{\lfloor 1'} + \overbrace{(a_1^2a_7 - 2a_1a_5)}^{E}\,\overset{\mathrm{f}}{T}{}^{\lfloor n2}_{\lfloor 1'} + \overbrace{(2a_1a_5a_7 - a_5^2)}^{F}\,\overset{\mathrm{f}}{T}{}^{\lfloor n}_{\lfloor 1'} \\ & \quad + \overbrace{(a_5^2a_7)}^{G} = A\overset{\mathrm{f}}{T}{}^{\lfloor n2}_{\lfloor 1'} + B\overset{\mathrm{f}}{T}{}^{\lfloor n}_{\lfloor 1'} + C, \\ & \overset{\mathrm{f}}{T}{}^{\lfloor n3}_{\lfloor 1'}D + \overset{\mathrm{f}}{T}{}^{\lfloor n2}_{\lfloor 1'}(E - A) + \overset{\mathrm{f}}{T}{}^{\lfloor n}_{\lfloor 1'}(F - B) + (G - C) = 0 \\ & \quad = f\left(\overset{\mathrm{f}}{T}{}^{\lfloor n}_{\lfloor 1'}\right). \end{aligned} \tag{37}$$

Newton's method can be used to find the zero of Eq. (37). Once the fluid-phase temperature function $\overset{\mathrm{f}}{T}{}^{\lfloor n}_{\lfloor 1'}$ is found satisfying Eq. (37), $p^{\lfloor n}_{\lfloor 1}$ may be determined from Eq. (32). Automatically $p^{\lfloor n}_{\lfloor 1'} = p^{\lfloor n}_{\lfloor 1}$. The solid-phase temperature $\overset{\mathrm{s}}{T}{}^{\lfloor n}_{\lfloor 1'}$ is found from Eq. (34). For transpiration from the regenerator to the refrigerator the boundary conditions are obtained by interchanging the primed and unprimed indices.

The energy wall balance, Eq. (19), is discretized using a simple forward time integration:

$$\begin{aligned} \frac{T_{\mathrm{w}}^{\lfloor n} + 1 - T_{\mathrm{w}}^{\lfloor n}}{\Delta t} = {} & \left(\frac{h_{\mathrm{c_{sw}}}(1-\phi)A_{\mathrm{c}}}{c_{\mathrm{w}}\rho_{\mathrm{w}}V_{\mathrm{w}}}\right)\left[\overset{\mathrm{s}}{T}{}^{\lfloor n}_{\lfloor N} - T_{\mathrm{w}}^{\lfloor n}\right] \\ & + \left(\frac{h_{\mathrm{c_{fw}}}\phi A_{\mathrm{c}}}{c_{\mathrm{w}}\rho_{\mathrm{w}}V_{\mathrm{w}}}\right)\times\left[\overset{\mathrm{f}}{T}{}^{\lfloor n}_{\lfloor N} - T_{\mathrm{w}}^{\lfloor n}\right] \\ & - \left(\frac{h_{\infty}A_{\mathrm{f}}}{c_{\mathrm{w}}\rho_{\mathrm{w}}V_{\mathrm{w}}}\right)\left[T_{\mathrm{w}}^{\lfloor n} - T_{res}\right]. \end{aligned} \tag{38}$$

The solid-phase/wall boundary condition Eq. (17), and the approximate fluid-phase/wall boundary condition Eq. (18) are discretized as follows:

$$\begin{aligned} & \overset{\mathrm{s}}{T}{}^{\lfloor n}_{\lfloor N}\left[1 + \left(\frac{2\Delta\xi h_{\mathrm{c_{sw}}}\mathscr{J}^{\lfloor n}_{\lfloor N}}{3k_{\mathrm{s}}}\right)\right] \\ & \quad = \left(\frac{2\Delta\xi h_{\mathrm{c_{sw}}}\mathscr{J}^{\lfloor n}_{\lfloor N}}{3k_{\mathrm{s}}}\right)T_{\mathrm{w}}^{\lfloor n} + \frac{4}{3}\overset{\mathrm{s}}{T}{}^{\lfloor n}_{\lfloor N-1} - \frac{1}{3}\overset{\mathrm{s}}{T}{}^{\lfloor n}_{\lfloor N-2} \\ & \overset{\mathrm{f}}{T}{}^{\lfloor n}_{\lfloor N}\left[1 + \left(\frac{2\Delta\xi h_{\mathrm{c_{fw}}}\mathscr{J}^{\lfloor n}_{\lfloor N}}{3k_{\mathrm{f}}}\right)\right] \\ & \quad = \left(\frac{2\Delta\xi h_{\mathrm{c_{fw}}}\mathscr{J}^{\lfloor n}_{\lfloor N}}{3k_{\mathrm{f}}}\right)T_{\mathrm{w}}^{\lfloor n} + \frac{4}{3}\overset{\mathrm{f}}{T}{}^{\lfloor n}_{\lfloor N-1} - \frac{1}{3}\overset{\mathrm{f}}{T}{}^{\lfloor n}_{\lfloor N-2} \end{aligned} \tag{39}$$

Eqs. (38) and $(39)_{1,2}$ apply to both reactors, with primed space indices suppressed for the regenerator.

6. Discussion

The ability of the adaptive scheme to calculate and integrate the source terms was assessed by comparing a moving grid calculation ($N = 26$) with two stationary, uniformly spaced calculations: one with the same number of nodes, and a fine-zoned fixed grid reference calculation ($N = 51$). The grid function used was (WFGRADLN), Eq. (5). Results are compared during two different phases (preheating and precooling), as discussed in the introduction. The grid constants used were $\mathscr{J}_{\min} = 0.65$ and $\beta = 8 \times 10^{-4}$; the latter value was chosen based upon gradients estimated from the fixed grid calculation during the precooling phase. A complete description of the reactor parameters and the equilibrium metal hydride models is given in (Lloyd et al. 1998,2001; Lloyd, 1998).

Fig. 6a and b show the source term $\dot{\varphi}$, which is a function of $\partial x/\partial\tau|_{\xi}$ (i.e., Eq. (27)), during the preheating phase (step one). Fig. 6a is the fixed grid calculation and Fig. 6b the moving grid. During the preheating phase heat (at $T_{\mathrm{hot}} = 150$ °C) is applied to the reactor. This promotes an inward moving desorption front.

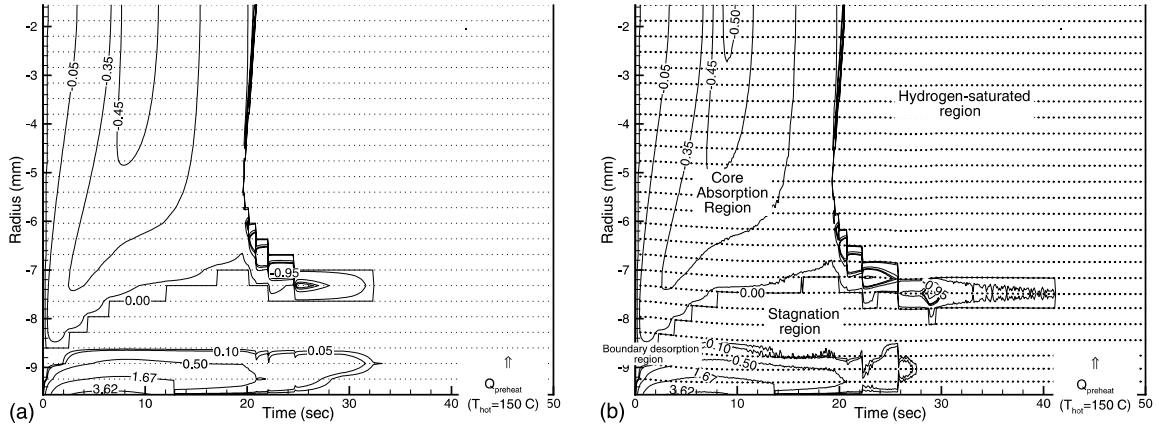

Fig. 6. Mass source term $\dot{\varphi}$ ($\mathrm{kg_{H_2}/m^3_{(c)}\,s}$) and grid trajectories in the regenerator during the preheating phase. (a) fixed grid, $N = 26$. (b) moving grid, $N = 26$, with $\mathscr{I}_{\min} = 0.65$ and $\beta = 8 \times 10^{-4}$. (Note: stepped contours result from termination of kinetics—as from complete absorption or desorption or a local state of equilibrium—in conjunction with the finite grid size.)

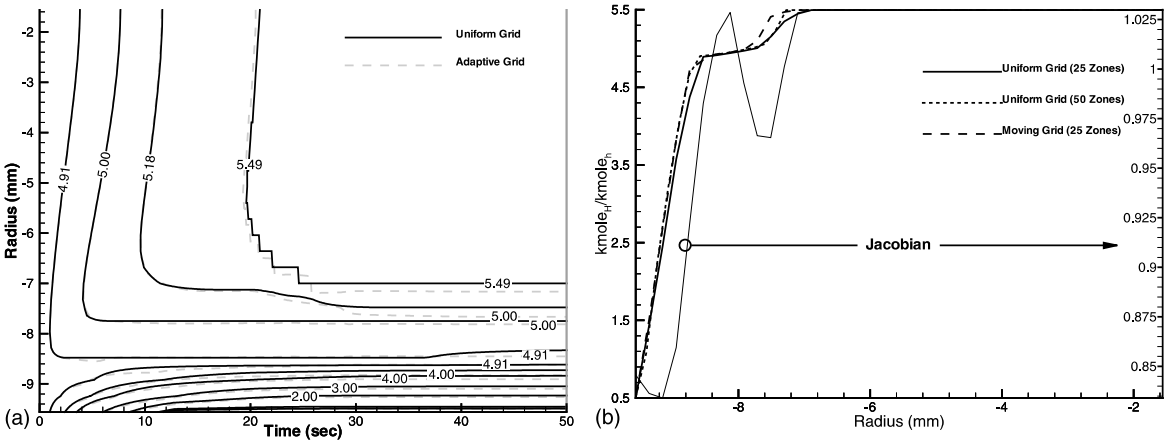

Fig. 7. (a) Contours of absorbed hydrogen concentration, x ($\mathrm{kmol_H/kmol_h}$), in the preheating step, for fixed and moving grids, $N = 26$. (b) concentration profiles at $t = 40$ s, all three calculations.

Reabsorption in the core region continues until the limiting concentration $x = x_{\beta_{\min}} = 5.5$ ($\mathrm{kmol_H/kmol_h}$) is reached, at which point further evolution is greatly retarded. The grid trajectories are shown in Fig. 6b. As can be seen, the moving grid does not alter the basic desorption field.

The concentration profiles during the preheating phase are overlain in Fig. 7a. The only observable difference is that the moving grid calculation predicts a stagnation front situated closer to the reactor wall. To see this difference more clearly, the concentration profiles at $t = 40$ (s) are shown in Fig. 7b, which also includes the result from the reference calculation ($N = 51$). Fig. 7b demonstrates that the concentration profile which develops during this phase is indeed a monotonic one, and under this situation the moving grid calculation is evidently able to capture the gradient in the boundary desorption region quite accurately (with respect to the $n = 50$ fixed grid reference calculation) using one half the number of grid points. The difference in the location of the smaller front at $r = 7$ (mm) is likely due to expansion of the grid between the two fronts, as indicated by the grid Jacobian in Fig. 7b, indicating that modification of Eq. (5) to include curvature is desirable.

During the preheating step the refrigerator reactor domain is uncoupled from the regenerator, and normally remains in equilibrium, with $\overset{\mathrm{s}}{T} = \overset{\mathrm{f}}{T} = 20$ °C, $p = p_{\mathrm{eq}}$, until the start of the second step. This circumstance was used to check for spurious source terms by setting the grid velocities in the refrigerator to mirror those of the regenerator (whereas otherwise they would be zero to machine precision). The result of this procedure is shown in Fig. 8. Fig. 8a shows the mirrored grid Jacobian field; Fig. 8b shows corresponding $\dot{\varphi}$ and velocity fields, which indeed remain zero in the refrigerator. This test indicated that the discretization produced no spurious source terms and satisfies the uniformity constraint mentioned earlier.

Considerably larger gradients as well as more complicated reaction fronts develop during the precooling

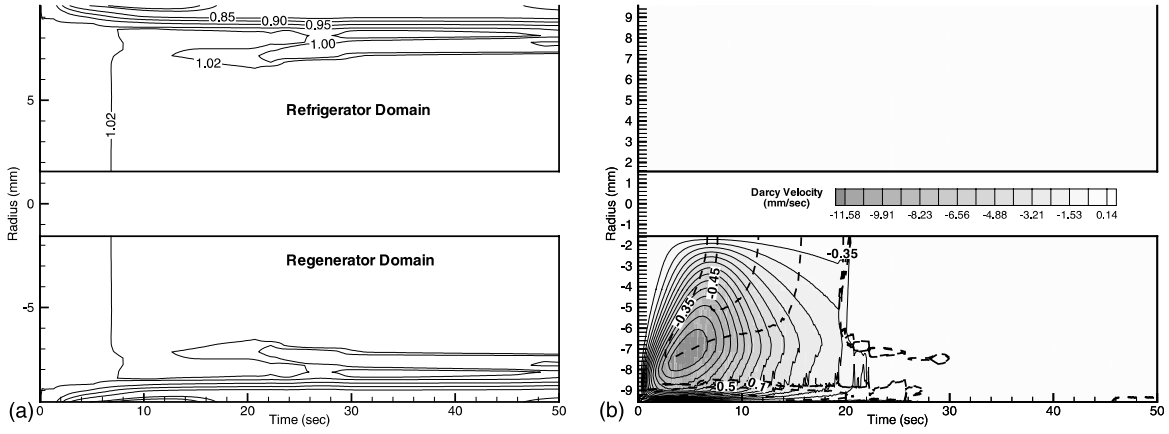

Fig. 8. Effect of grid motion in the regenerator and refrigerator during the preheating phase, $N = 26$. Domains are uncoupled and in the refrigerator is static, with the grid swept by imposed the grid motion of the regenerator. (a) Grid Jacobians, (b) mass source fields and velocity fields (dotted lines).

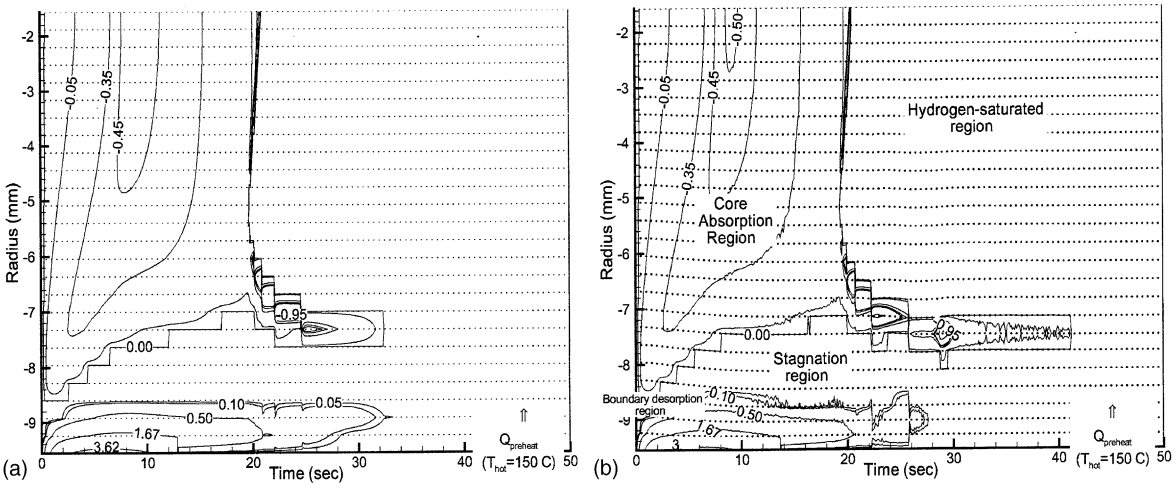

Fig. 9. Mass source term $\dot{\varphi}$ ($kgH_2/m^3_{(c)}$ s) and grid trajectories in the regenerator during the precooling phase. (a) fixed grid, $N = 26$, (b) moving grid, $N = 26$, with $\mathscr{J}_{\min} = 0.65$ and $\beta = 8 \times 10^{-4}$.

phase. During this phase, the reactors are also isolated and the hot regenerator is brought to ambient temperature, $T = 20$ °C. The monotonic profile in the regenerator developed during the preheating step (and maintained during the charging step, when the reactors are coupled) is lost as the hot reactor is coupled to ambient temperature. Absorption commences at the wall boundary and an absorption skin accumulates rapidly, favored by the relatively low heat transfer resistance from the wall to the ambient reservoir. Concurrent desorption from the core region also requires heat transfer in order to be sustained. The competing effects of heat transfer inward to the core to sustain desorption ($\dot{\varphi} > 0$), and heat transfer outward from the wall skin to the sustain wall absorption ($\dot{\varphi} < 0$), lead to the wide stagnation region where $\dot{\varphi} = 0$, clearly apparent in the fixed grid calculation (Fig. 9a) and are ultimately the source of the development profile between $5.56 < r < 8$ mm, shown in Fig. 10b.

Fig. 9a and b show the mass source fields for the fixed grid and moving grid cases, respectively. The corresponding concentration fields are overlain in Fig. 10a; snapshots illustrating the evolution of the concentration profiles from a monotonic desorption gradient to an inward moving front with high curvature are shown in Fig. 10b.

Comparison of the two source fields shows similarity in general, but significant local differences, which may broadly be characterized as oscillations of the stagnation region. The overall effect is to smooth the concentration profile. This oscillation is a numerical artifact arising from the purely gradient-based algorithm. With reference to Fig. 11a, as the wall skin first appears, $\partial x/\partial r|_{\text{wall}}$ is initially negative, decreases through zero, and becomes positive. The grid algorithm reflects the zero gradient inflection in the concentration profile by redistributing the grid away from the wall—the cause of the upward spike in the Jacobian in Fig. 11a at $t = 126$ s.

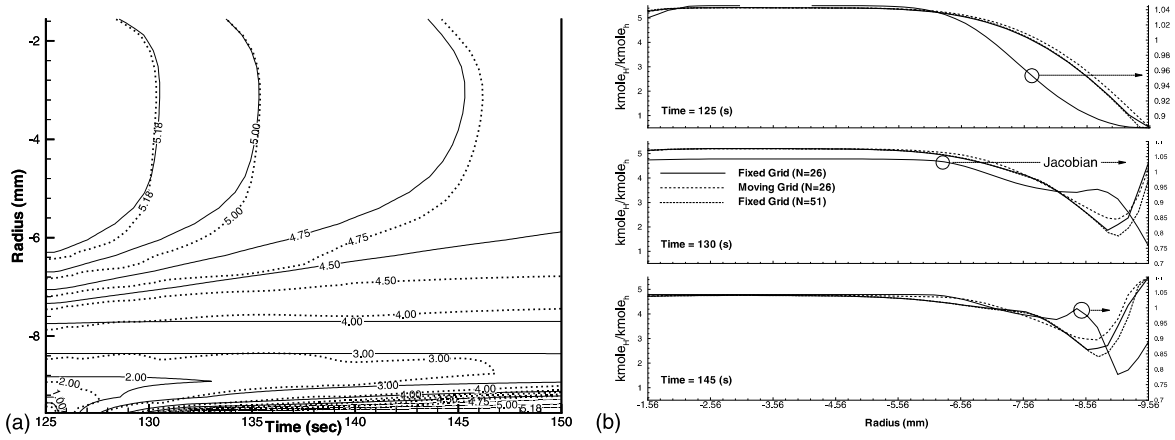

Fig. 10. (a) Comparison of concentration contours, (b) comparison at selected times.

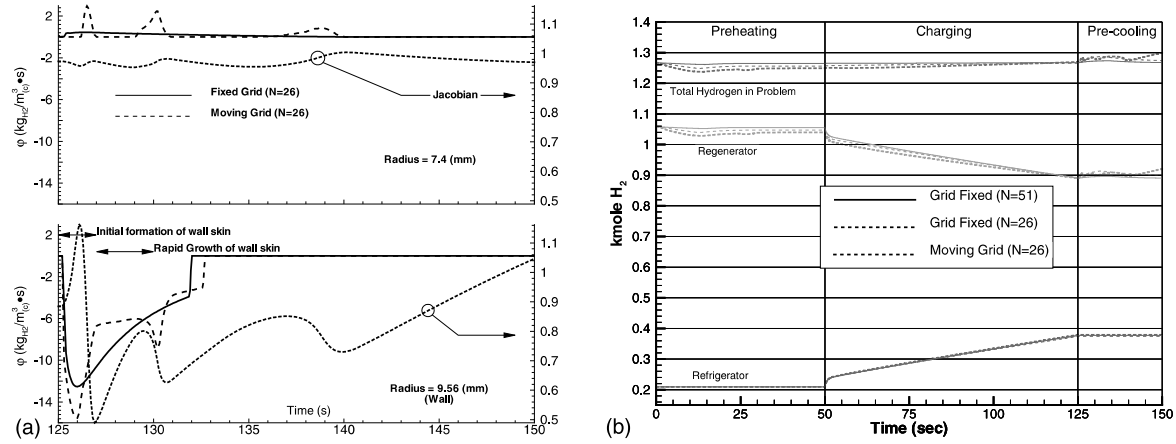

Fig. 11. (a) Mass source term at two radii for fixed and moving grid, $N = 26$ (see Fig. 9a and b). (b) Comparison of reactor hydrogen inventories for fixed grid ($N = 26$ and 51) and moving grid, $N = 26$.

Hence, an unfortunate effect of the gradient-based scheme is that resolution of the source fields is reduced. As the wall skin accumulates, the grid density in the wall region increases, to a minimum Jacobian of 0.5 (which may be compared with the set value of $\mathscr{J}_{\min}$).

The increased grid concentration near the wall enables the moving grid calculation to capture the second inflection in the profile which occurs after $t = 130$ s, and is clearly evident in Fig. 11b at the time, $t = 145$ s. The "rounding" of the concentration profile at the wall is predicted by the $N = 51$ fixed grid result, but not resolved by the $N = 26$ fixed grid result. It is, however, picked up by the $N = 26$ moving grid calculation. This, too, has the same unfortunate effect of decreasing the grid density near the wall. This is the source of the absorption spike at about 139 s.

Finally, in order to judge these results from a different perspective we note that a numerical scheme must also satisfy conservation laws over finite times. The relative merit of the different schemes to do so were assessed by examining the total reactor hydrogen concentration as a function of time; these comparisons are shown in Fig. 11b. Clearly, the fine-zoned fixed grid calculation satisfies mass conservation for both single and coupled domains to a high degree of accuracy. Additionally, all calculations appear to perform equally well in the refrigerator domain, perhaps due to the much smaller gradients there (i.e., refer to Fig. 1b).

7. Closure

This paper has compared results from a gradient-based adaptive moving grid method to results obtained using uniform, fixed grids. The problem of interest includes strong, localized mass and energy source terms, and both monotonic reaction fronts as well as those exhibiting curvature are present. The discretization is consistent, second-order accurate, and was demonstrated to be mass conserving. Convergence of the fixed grid solution was demonstrated by mesh refinement.

In the case of a *monotonic* concentration gradient occurring during preheating, the comparison showed excellent agreement between the fixed grid results and the moving grid study. Further, the moving grid scheme was able to compute the reaction front gradient which was achieved only with a fixed grid having twice as many points.

However in the presence of more complicated features exhibiting curvature during precooling, the gradient-based weight function appeared to degrade accuracy and distort the mass source field, promoting spatial-temporal oscillations which smoothed the concentration profile. Diagnostics based upon correlating the grid Jacobian with the difference between the moving grid and fixed grid calculations indicates that where differences exist, they arose in regions of high curvature of the concentration profile, or in regions where large mass source terms were present in conjunction with small gradients, reducing the resolution for the source terms.

On the basis of these results, we propose that grid weight functions for this class of problems be extended to incorporate both curvature and measures directly related to the source terms.

References

Bains, M.J., 1998. Grid adaptation via node movement. Appl. Numer. Math. 26, 77–96.

Bieniaz, L.K., 1993. Use of dynamically adaptive grid techniques for the solution of electrochemical kinetic equations. Part I. J. Electroanal. Chem. 360, 119–138.

Crowley, 1967. PUFL, an almost Lagrangian gasdynamic calculation for pipe flows with mass entrainment. J. Comput. Phys. 2 (1), 61–85.

Dang, Vu.C., Delcambre, B., 1987. Etude Expérimentale et Modélisation d'un Stockage Thermique de Longue Durée en Lit de Cailloux Enterré, Couplé à des Capteurs Solaires à Air. Rev. Phys. Appl. 22, 487–503.

Daripa, P., 1992. Iterative schemes and algorithms for adaptive grid generation. J. Comput. Phys. 100, 284–293.

Farrell, K., Drury, L., 1998. An explicit, adaptive grid algorithm for one-dimensional initial value problems. Appl. Numer. Math. 26 (1/2), 3–12.

Frauhammer, J., Klein, H., Eigenberger, G., Nowak, U., 1998. Solving moving boundary problems with an adaptive moving grid method: rotary heat exchangers with condensation and evaporation. Chem. Eng. Sci. 53 (19), 3393–3411.

Fukuda, K., Tetsuya, K., Haseqawa, S., 1992. Similarity rule between heat transfer and pressure drop of porous material. AIChE J. 38 (11), 1840–1842.

Huang, W., Russell, R.D., 1999. Moving mesh strategy based on a gradient flow equation for two dimensional problems. SIAM J. Sci. Comput. 20 (3), 998–1015.

Kaviany, M., 1995. Principles of Heat Transfer in Porous Media, second ed. Springer-Verlag, New York.

Kim, K.J., Feldman, K.T., Lloyd, G., Razani, A., Shanahan, K.L., 1998. Performance of high power metal hydride reactors. Int. J. Hydrogen Energy 23 (5), 355–362.

Knupp, P., Steinberg, S., 1994. Fundamentals of Grid Generation. CRC Press, Boca Raton.

Lawal, A., 1990. Adaptive grid method for convection–diffusion equations. Int. J. Heat Mass Transfer 33 (8), 1633–1641.

Liu, F., Ji, S., Liao, G., 1998. An adaptive grid method and its application to steady euler flow calculations. SIAM J. Sci. Comput. 20 (3), 811–825.

Lloyd, G.M., 1998. Optimization of heat and mass transfer in metal hydride systems. Ph.D. Thesis, University of New Mexico.

Lloyd, G., Razani, A., Feldman, K.T., 1995. Fundamental issues involved in a theoretical description of the heat and hydrogen transfer occurring in coupled porous metal hydride reactors. Proc. ASME Int. Mech. Eng. Cong. Exp., San Francisco HTD-321/FED-233, 671–681.

Lloyd, G., Razani, A., Feldman Jr., K.T., 1998. Transitional reactor dynamics affecting optimization of a heat-driven metal hydride refrigerator. Int. J. Heat Mass Transfer 41 (3), 427–513.

Lloyd, G., Razani, A., Kim, K.J., 1999. non-local thermal equilibrium computational results for reacting flow in two-phase gas/solid porous media. in: Proceedings of the ASME National Heat Transfer Conference, August 15–17, 1999, Albuquerque, New Mexico, "Numerical Methods for Porous Media".

Lloyd, G., Razani, A., Kim, K.J., 2001. The influence of source terms on a gradient-based curvilinear grid scheme applied to a non-local thermal equilibrium reacting flow. in: Proceedings: ICHMT, International Symposium on Advances in Computational Heat Transfer, Computational and Mathematical Methods, Palm Cove, Queensland May 20–25, 2001, pp. 493–501.

Mackenzie, J.A., Robertson, M.L., 2000. The numerical solution of one-dimensional phase change problems using an adaptive moving mesh method. J. Comput. Phys. 161, 537–557.

Reid, C.R., Oakberg, R.G., 1990. A continuum theory for the mechanical response of materials to the thermodynamic stress of sintering. Mech. Mater. 10, 203–213.

Strikwerda, J.C., 1989. Finite Difference Schemes and Partial Differential Equations. Chapman & Hall, London.

White, F.M., 1991. Viscous Fluid Flow, second ed. McGraw-Hill Inc, New York, p. 50.

Yasar, O., Moses, G.A., 1992. Explicit adaptive grid radiation-magnetohydrodynamics. J. Comput. Phys. 100, 38–49.